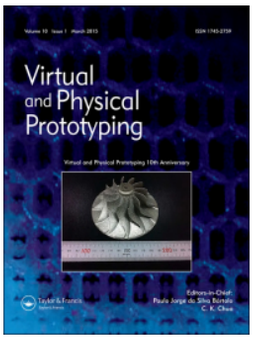

Taylor & Francis
Taylor & Francis Group

Virtual and Physical Prototyping

ISSN: 1745-2759 (Print) 1745-2767 (Online) Journal homepage: www.tandfonline.com/journals/nvpp20

Multi-sensor monitoring for optimising printing parameters of laser powder bed fusion (L-PBF) processes

Allen Hum Jun Wee, Qing Yang Lu, Truong Do, Ngoc Vu Nguyen & Tuan Tran

To cite this article: Allen Hum Jun Wee, Qing Yang Lu, Truong Do, Ngoc Vu Nguyen & Tuan Tran (2025) Multi-sensor monitoring for optimising printing parameters of laser powder bed fusion (L-PBF) processes, Virtual and Physical Prototyping, 20:1, e2511118, DOI: 10.1080/17452759.2025.2511118

To link to this article: https://doi.org/10.1080/17452759.2025.2511118

Published online: 22 Jun 2025.

VIRTUAL AND PHYSICAL PROTOTYPING
2025, VOL. 20, NO. 1, e2511118 (16 pages)
https://doi.org/10.1080/17452759.2025.2511118

Taylor & Francis
Taylor & Francis Group

Multi-sensor monitoring for optimising printing parameters of laser powder bed fusion (L-PBF) processes

Allen Hum Jun Wee [a], Qing Yang Lu[a], Truong Do [b], Ngoc Vu Nguyen [a] and Tuan Tran [a]

[a]School of Mechanical and Aerospace Engineering, Nanyang Technological University, Singapore, Singapore; [b]College of Engineering and Computer Science, VinUniversity, Hanoi, Vietnam

ABSTRACT

Laser powder bed fusion (L-PBF) is widely recognised as a reliable technology for metal additive manufacturing (AM). However, industrial adoption of this technology still requires established methods to ensure its products' quality and optimise its printing parameters, either using in-process monitoring data or post-process characterisation. In this study, we utilise both visible-light and thermal imaging sensors to monitor L-PBF processes and provide a quantitative characterisation of the printed layers. For each layer of a printed part, we use a combination of thermal information and surface appearance to develop quality indicators capable of distinguishing printed parts with acceptable quality and those prone to overheating and lack of fusion. We also demonstrate the use of these quality indicators in detecting thermal deformation for overhanging structures.

ARTICLE HISTORY
Received 17 February 2025
Accepted 11 May 2025

KEYWORDS
Powder bed fusion; in-process monitoring; visible-light imaging; thermal imaging; anomaly detection

1. Introduction

Additive manufacturing (AM) is one of the fast-growing and dynamic markets with the most revenue returned for automobile, medical and consumer electronics. AM also has the potential to disrupt the supply chain management system by substantially reducing stockpiles and supplier base [1]. Benefits of AM for metal fabrication include (1) mass customisation of products, (2) fabrication of complex geometries within a single process, and (3) production of dense parts with mechanical performance approaching that of bulk material. Nonetheless, the wide adoption of metal AM has been hindered by several major issues originating from a lack of standardisation and quality control of the printed products.

Laser powder bed fusion (L-PBF) is widely regarded as a reliable process for metal AM. Generally, L-PBF involves numerous process parameters, e.g. laser power, scanning speed, gas flow rate, and beam diameter. The occurrence of defects is inevitable if any of the process parameters are inappropriately chosen. The process parameters therefore must be heuristically tuned as they strongly depend on structural designs and materials. This causes uncertainties in controlling the printed product's reproducibility and quality. There are more than 50 parameter variations that may cause significant deviations in the quality of printed products [2]. Another challenge is the lack of well-defined international standards for metal AM products. Current practices in inspecting AM specimens rely on non-destructive tests, e.g. X-ray computed tomography (CT), an approach that is both time-consuming and costly.

To address the lack of quality control and standardisation in metal AM, various in-process monitoring systems have been introduced in recent years. One of the earliest efforts to acquire monitoring information during the printing process was carried out using co-axial setups in which the optical path to monitoring sensors is coupled to the laser path. CMOS cameras and photodiodes were used to measure the melt pool dimension and intensity [3]. Both the CMOS cameras and the photodiodes were aligned to the laser path via a beam splitter. The results indicated that the stability of the melt pool was essential for the sintering of powder. The same principle was applied using an infrared camera to analyze the melt pool behaviours [4]. Despite a good correlation between the melt pool dynamics and the scan track, the depth variation of the scan track was difficult to probe, and there was a lack of understanding of the penetration depth.

Besides co-axial systems, the off-axial counterparts have been widely used as they typically offer a larger

CONTACT Tuan Tran ttran@ntu.edu.sg School of Mechanical and Aerospace Engineering, Nanyang Technological University, 639798, Singapore; Truong Do truong.dt@vinuni.edu.vn College of Engineering and Computer Science, VinUniversity, Hanoi, Vietnam

field of view (FOV). Furthermore, they have the capability to register data in the build-up direction (Z-axis). Off-axial systems consisting of a camera with a resolution of 36.3 megapixels were used to capture the powder bed with modulus-controlled illuminators for different signatures [5]. Images were captured for each layer both after laser scanning and after powder deposition. The system was capable of capturing signatures such as drag tracing caused by damages to the recoater blade, inhomogeneous powder distribution and part elevation. Furthermore, the built-up data were used to create three-dimensional (3D) models and subsequently to identify the defect locations. Similarly, the use of a high-speed camera in an off-axis setup to monitor the powder bed was demonstrated [6]. A threshold image acquisition rate of 300 frames per second (FPS) was identified to detect any anomaly signatures occurring in the melt pool during laser scanning. Besides identifying anomalous signatures, they also showcased the reconstruction of a volumetric model from layer-wise data to determine the location of the anomalies. High-speed cameras were utilised to detect keyhole porosity and balling phenomenon [7]. In comparison to co-axial systems, it was demonstrated that off-axis systems could identify more anomalous signatures, e.g. balling, spatters, plume and geometric deformation [8, 9]. An off-axis optical system and a trained deep learning network were used to monitor part surfaces after each layer deposition, enabling the detection of defects, e.g. lack-of-fusion, overheating, and warpage [10, 11].

The choice of imaging sensors is also crucial for the development of in-process monitoring systems. Deviations of process parameters from optimal values may lead to adverse fluctuations in the temperature of the melt pool that could cause printing anomalies and potential defects in printed parts. As a result, thermal imaging sensors were adopted to monitor the heat-affected zone (HAZ) in the powder bed during laser scanning beside visible-light imaging sensors. The spatial and temporal evolution of the HAZ was evaluated using an infrared (IR) camera mounted off-axially to monitor a region of 160 mm $\times$ 120 mm in the powder bed [12]. The HAZ area was demonstrated to increase proportionally with laser power and powder thickness, an observation pointing to instabilities in the melt pool. The use of an IR camera was illustrated in an off-axis configuration to monitor a region of 250 mm $\times$ 250 mm to detect lack of fusion and keyhole defects [13]. This approach enabled an 80% accuracy of detecting lack of fusion and 33% of keyhole defect detection. The formation of keyhole defects, which often occurred several layers below the powder bed's top surface, was the underlying cause of the reduced probability of their detection. Nonetheless, a limitation of using thermal imaging sensors for detecting anomalous signatures is the inability to probe those unrelated to thermal effects, e.g. damaging of the recoated blade, or those occurring below the monitoring layer.

In this study, we propose a quantitative framework that fuses visible-light and thermal imaging data to formulate layer-wise quality indicators for L-PBF processes. These indicators quantitatively characterise the surface condition and thermal history at each layer. The applicability of the proposed quality indicators is demonstrated on overhanging structures, a common and industrially relevant geometry in complex L-PBF parts. This approach provides a foundation for real-time detection of surface anomalies and defects during L-PBF processes. In Section 2, we describe the experimental setup and methods to capture printing anomalies. In Section 3, we focus on details of the data-processing algorithms and a data fusion approach to correlate data from both sensors for the identification of anomalous signatures. In Section 4, we present the results obtained by the proposed data fusion approach and finally conclude the paper in Section 5.

2. Experimental methods

2.1. Experimental setup

Our experiments were conducted using a commercial L-PBF machine (500-HL, SLM Solutions) with a build envelope of 500 $\times$ 280 $\times$ 365 mm. The build layer thickness for all our experiments is set at 50 μm. The laser beam spot diameter is approximately from 80 μm to 120 μm, allowing minimum build features of 150 μm. The build platform is pre-heated to 200°C prior to printing to lessen the thermal gradient and the resulting thermal stress in printed parts.

We use our in-process monitoring system (IMS) consisting of a visible-light imaging (VI) camera, a thermal imaging (TI) camera, a dichroic mirror, and a deflector to capture images of printed layers during the printing process [14]. Figure 1 depicts the schematic of our off-axis experimental setup of the IMS. The build chamber is illuminated by 9 strips of LED, each 48 W, to provide even illumination. Reflected light from the powder bed is allowed to go through the chamber's viewport made of Calcium Fluoride with transmission wavelength from 0.25 μm to 7 μm. It is then directed to the dichroic mirror by a deflector. The dichroic mirror directs light in the visible and infrared ranges to the VI and TI cameras, respectively.

The VI camera (D850, Nikon) with sensor size of 8256 $\times$5504 pixels is attached to a 200 mm lens (AF

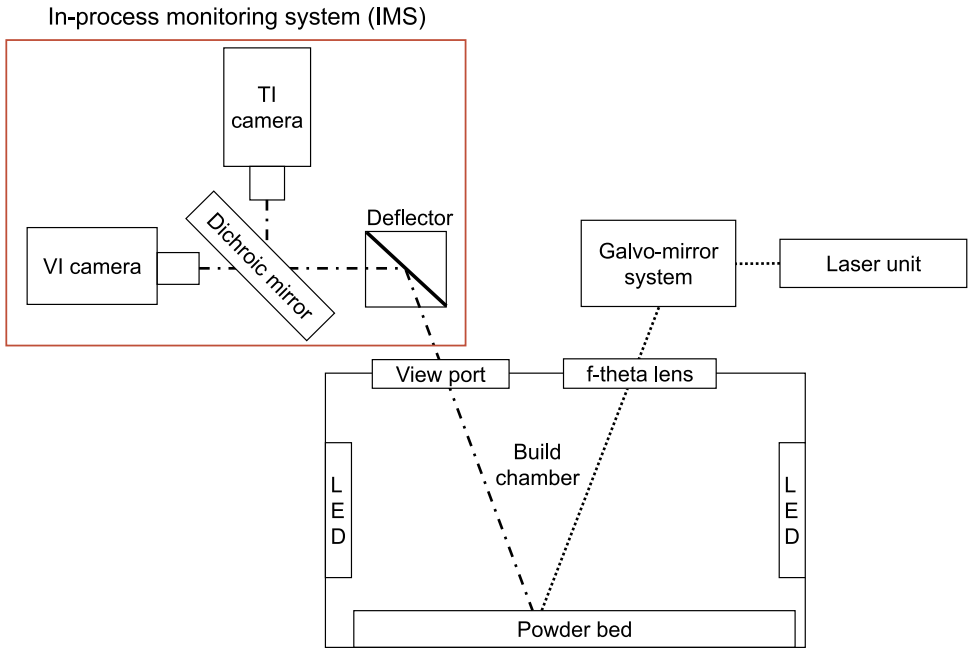

Figure 1. Schematic of the in-process monitoring system (bounded by the red box) and the SLM printer.

Micro-Nikkor, Nikon) to achieve a field of view (FOV) of 65 × 40 mm. The TI camera (ImageIR® 8355, InfraTec) operates with light in mid IR range, from 2 μm to 5.7 μm, and has a sensor size of 640 × 512 pixels. The TI camera is attached to a lens of 25 mm focal length to achieve a FOV of 165 × 100 mm. Both cameras have the same working distance of approximately 500 mm. Measurement of the modular transfer function using a USAF 1951 resolution target results in an optimum f-number of f/22 for the AF Micro-Nikkor lens with a corresponding spatial resolution of 35 μm/pixel [14]. The lens used for the TI camera has a fixed f-number and a spatial resolution of 195 μm/pixel.

In our in-process monitoring experiments, the VI camera captures two images of the powder bed for each printed layer: (1) after laser scanning (ALS) and (2) after the recoater blade recoats powder (AFR). The camera is automatically triggered by a photo-interrupter installed near the recoater 'home' position: a signal is generated when the recoater either departs from or returns to the 'home' position, thereby triggering the VI camera to capture an ALS image or an AFR image, respectively. The TI camera records the printing process at a constant frame rate of 25 FPS.

Image alignment: To align images obtained by the VI and TI cameras, we use a chessboard consisting of 10 × 10 mm silver grids printed on thermoplastic. The chessboard is placed on a heated platform of 50°C, allowing both the VI and TI cameras to simultaneously capture the grids with sufficient contrast. The images of the chessboard taken by both the VI and TI cameras are used for the image registration process described in Section 3.1.

Thermal image calibration: Typically, error in temperature measurement of the TI camera arises from temperature drift caused by the optical components of the experimental setup and the unknown emissivity of the printed specimen. We correct the temperature drift caused by optical components of the experimental setup using a blackbody simulator (BX-500, CEM) as the thermal imaging target. The transmission coefficient of the optical components measured by the blackbody simulator is 0.044. To measure the emissivity of specimens printed using different parameter settings, we uniformly heat these specimens to a temperature of 250°C and use a calibrated thermocouple as a reference. The emissivities corresponding to different parameter settings are shown in Table 1.

The average emissivity of the specimens across the 10 parameter settings used in our experiment is 0.238. Multiplying this average emissivity by the transmission

Table 1. Emissivities of specimens printed using parameter settings shown in Table 2.

Parameter setting	$\mathbb{P}_1$	$\mathbb{P}_2$	$\mathbb{P}_3$	$\mathbb{P}_4$	$\mathbb{P}_5$	$\mathbb{P}_6$	$\mathbb{P}_7$	$\mathbb{P}_8$	$\mathbb{P}_9$	$\mathbb{P}_{10}$
Emissivity	0.27	0.3	0.23	0.25	0.21	0.24	0.22	0.22	0.2	0.24

coefficient of the optical components yields an effective emissivity of approximately 0.011.

2.2. Design of experiments and data acquisition

We use stainless steel (SS) 316L powder, with particle diameters ranging from 20 μm to 53 μm, to print specimens with systematically varied parameter settings, as shown in Table 2. The baseline laser power and scanning velocity are denoted as P_0 and V_0, respectively. The energy density resulting from the use of P_0 and V_0 is referred to as the baseline energy density and denoted as E_0. Ten parameter settings were selected from a 4×4 matrix to cover a broad range of energy densities, from $0.5E_0$ to $4E_0$, allowing comparison across low, baseline, and high energy input conditions. The selected parameter settings provide sufficient variation while keeping the number of test cases efficient for systematic evaluation.

Table 2. Parameter settings used in our study.

Parameter setting	Laser power (W)	Scanning velocity (mm/s)	Energy density (J/mm^3)
$\mathbb{P}_1$	87.5	550	$0.5E_0$
$\mathbb{P}_2$	175	1100	$0.5E_0$
$\mathbb{P}_3$	175 (P_0)	550 (V_0)	45 (E_0)
$\mathbb{P}_4$	350	1100	E_0
$\mathbb{P}_5$	175	367	$1.5E_0$
$\mathbb{P}_6$	263	550	$1.5E_0$
$\mathbb{P}_7$	175	275	$2E_0$
$\mathbb{P}_8$	350	550	$2E_0$
$\mathbb{P}_9$	350	367	$3E_0$
$\mathbb{P}_{10}$	350	275	$4E_0$

We focus on evaluating the dependence of build quality on deposition energy density E, which is calculated using the laser power P, laser's scanning velocity v, hatch spacing h, and thickness T of the powder layer:

$$E = \frac{P}{vhT}. \tag{1}$$

We design and print two sets of specimens to identify and validate the signatures obtained by the multi-sensory monitoring system. The first set includes 10 circular cylinders of diameter and height 8 mm. Each cylinder is printed using a distinct parameter setting, detailed in Table 2. In Figure 2(a), we show the schematic of the specimens and their arrangement within the FOV of the

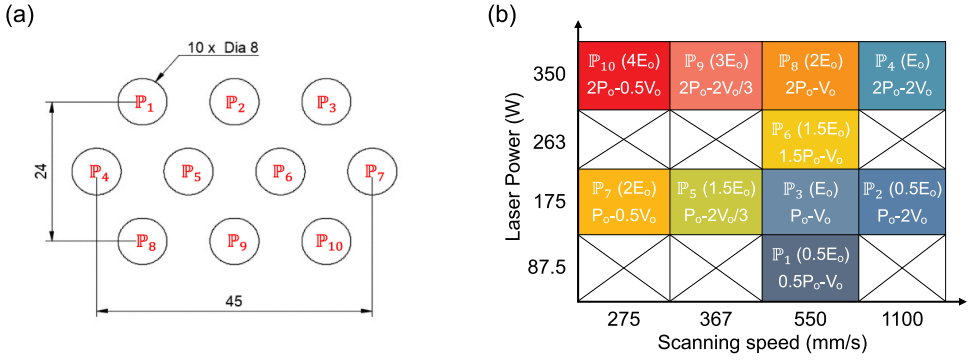

Figure 2. (a) Spatial arrangement of cylindrical specimens and the corresponding parameter settings. (b) Laser power and scanning velocity of different parameter settings.

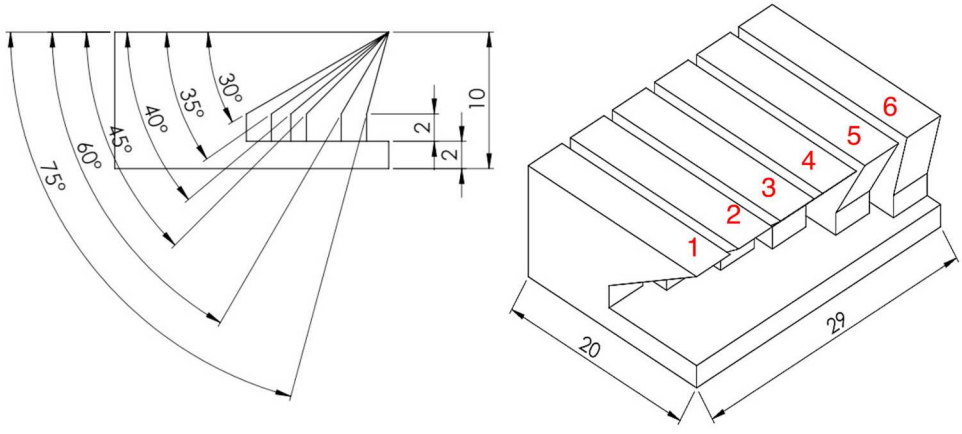

Figure 3. Design of overhanging structures with different overhanging angles α.

cameras. In Figure 2(b), we show how deposition energy density E varies for the parameter settings used in our experiment.

The second set of specimens consists of different overhanging structures with varying overhanging angles α, defined between the downward-facing surface of the stacked printing layers and the horizontal direction (Figure 3). We note that overhanging structures are prone to deformation during printing due to thermal stress. For printing of overhanging structures, we keep the parameter setting fixed at $\mathbb{P}_8$ ($P = 350\,\text{W}$, $v = 550\,\text{mm/s}$).

To validate the quality indicators identified through in-process monitoring, subsize dogbone tensile specimens were printed using the same ten parameter settings as the cylindrical specimens. The dimensions of the tensile specimens followed the ASTM E8/E8M-15a standard for tensile evaluation of metallic materials. For each parameter setting, three tensile specimens were tested under displacement control at a crosshead speed of 1 mm/min using a universal testing machine (Instron 5569, Instron).

3. Data processing

The acquired VI and TI images for each printed layer first are aligned in a pre-image processing step, namely image registration, before image processing and data analysis are carried out. Subsequently, the VI images of the printed surface and the mean temperature from the entire stack of TI images are obtained. All the algorithms for image processing are developed in MATLAB.

3.1. Pre-image processing and image registration

In the image registration step, images of the same scene but captured by different cameras or from different viewpoints are aligned to provide better correlation results. We note that numerous works have been reported on this topic, focussing on image registration for multiple sensing, pattern recognition, and robotic navigation. Invariant feature pairs (corners) from VI and TI images were used to determine the Hausdorff distance between the pairs of corners [15]. Image registration was performed using multi-level 1D wavelet decomposition followed by a translation [16]. Our approach is to detect all the checker points in the calibration grid images taken by the VI and TI cameras, followed by re-orientating and scaling the TI images to match the VI images. The corner points are determined using the gradient from adjacent pairs of checkpoints. The matched corner points of the VI and TI images determine the scaling, translation, shear and rotational factors of an affine transformation that transforms TI images to match VI images. The algorithm for image registration is shown in Annex Figure A1. The corner points are used to determine the affine transformation matrix. In Figure 4, we show a successful image registration of a TI image onto a VI image.

3.2. Pre-image processing and segmentation of the region of interest via mask

For a fixed geometry, extracting the region of interest (ROI) is achieved by multiplying the image with a passive mask. However, in most cases, the geometry of a part may vary due to its intricate design or deformation caused by thermal stress. Under such consideration, ROI segmentation must be performed using an active mask. The active mask has been emphasised in numerous studies and was illustrated earlier for monitoring process signatures in AM during laser scanning [8]. We use the principle of snake contour [17] to create an active mask for every ALS image before applying

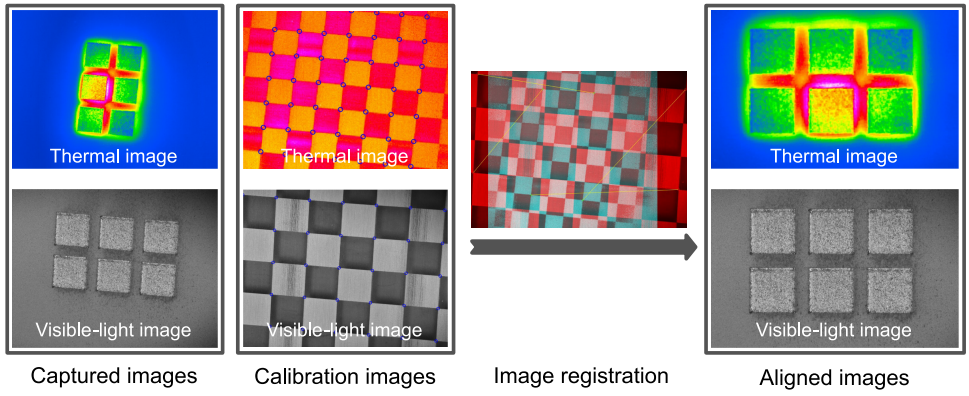

Figure 4. Image registration of a TI image onto a VI image.

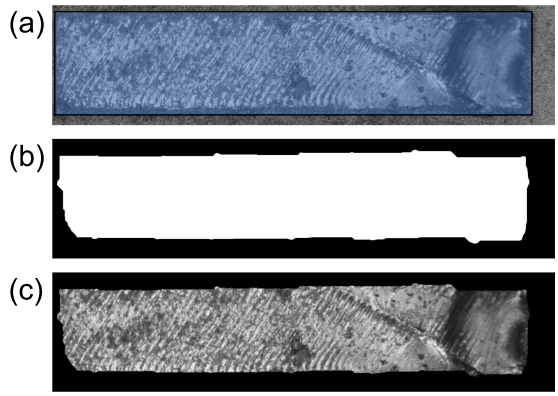

Figure 5. (a) A VI image of a layer after laser scanning. The area within the blue region is used to create an active mask. (b) A created active mask. (c) A VI image after applying the active mask.

image processing algorithms to determine the morphological information of the printed layer. Figure 5 illustrates the creation of an active mask.

3.3. Visible-light image processing

To obtain a quantitative assessment of the powder bed after laser scanning (ALS), we developed two image processing algorithms: (1) High Intensity Pixel Enhancement (HiPE) and (2) Low Intensity Pixel Enhancement (LoPE). These algorithms are designed to identify and highlight areas that are brighter or darker than the average intensity of the ROI, respectively.

Figure 6(a) illustrates how the HiPE algorithm is applied to an ALS image. First, the powder bed region is removed using a binary passive mask, which eliminates edge elevation caused by material buildup [18] and focuses on any possible anomaly within the specimen. This method conveniently removes any redundant regions. Subsequently, Gaussian filtering is applied to the ROI to remove sparse noise introduced by the experimental setup. Background subtraction is then performed to eliminate background disparity by subtracting the ROI from the powder bed image taken prior to the printing process. The contrast of the subtracted image is adjusted based on its maximum and minimum intensities, along with a weight factor of 0.3, which controls the maximum limit of the image contrast to be changed. An image exponential operation is applied to suppress pixels with low intensity values. Finally, a binarised image is obtained using Otsu thresholding.

The LoPE algorithm is similar to the HiPE algorithm except that an additional step is introduced at the beginning to invert the pixel values of the input image. Figure 6(b) illustrates the implementation of the LoPE algorithm on the same image used in Figure 6(a). Both the HiPE and LoPE algorithms for anomaly detection are shown in Annex Figures A2 and A3, respectively. For each layer l of a specimen, applying the HiPE algorithm to the area within the ROI generates a binary image with active pixels (those with a value of 1) associated with the areas having brighter shades. We denote the number of these active pixels resulting from the HiPE algorithm as $N_H(l)$. Similarly, using the LoPE algorithm on the same layer within the ROI results in the number of active pixels $N_L(l)$ associated with darker shades.

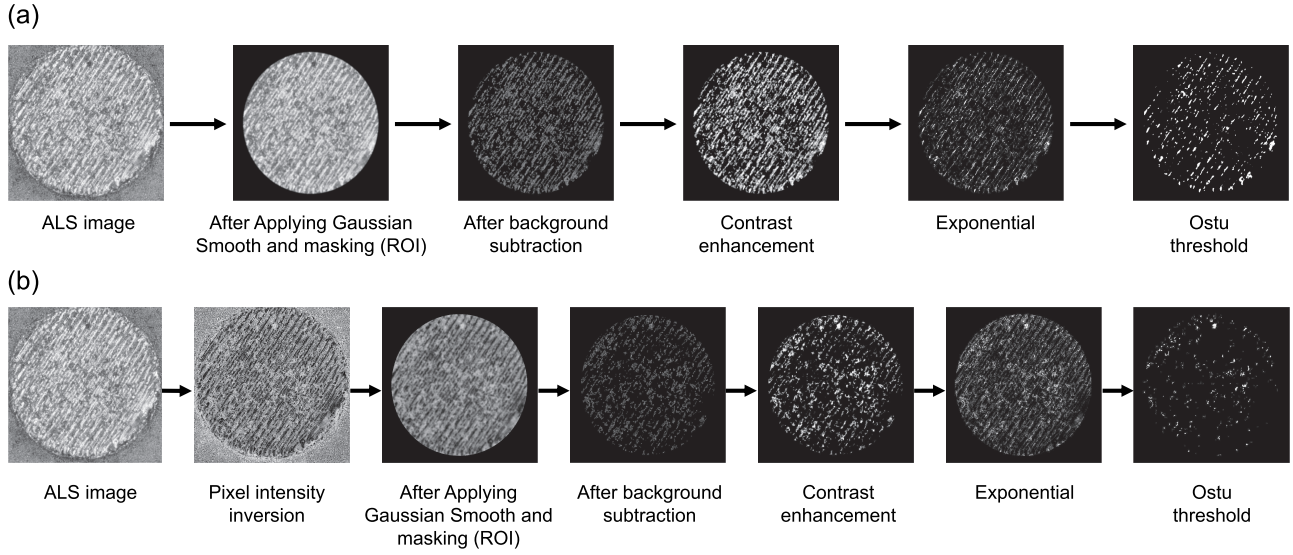

Figure 6. Illustration of (a) HiPE algorithm; (b) LoPE algorithm.

As a result, we calculate the ratio of active pixels (those with a value of 1) to the area $A(l)$ of the layer using each of these algorithms as

$$n_H(l) = \frac{N_H(l)}{A(l)}, \tag{2}$$

$$n_L(l) = \frac{N_L(l)}{A(l)}. \tag{3}$$

We note that the ratios n_H and n_L obtained by HiPE and LoPE for a certain layer represent the layer's brightness and darkness, respectively. These metrics may reveal surface irregularities or defects based on the powder bed conditions after laser scanning. On the one hand, an ideal ALS surface having mostly continuous laser-scanning tracks is associated with a higher value of n_H due to the higher reflectivity of sintered powder. The presence of balling, discontinuous tracks, or unsintered powder, all results in surface characteristics of lower reflectivity and leads to fewer active pixels and subsequently lower n_H in binarised HiPE images. On the other hand, applying the LoPE algorithm on an ALS image highlights darker regions, signifying anomalies such as overheating or redeposition of material. This causes an increase in n_L due to increasing number of active pixels in areas of potential thermal deformation.

We further quantify the ALS surfaces of a printed layer l by obtaining its normalised values of n_H and n_L as

$$\widehat{n}_H(l) = \frac{n_H(l) - \min(n_H)}{\max(n_H) - \min(n_H)}, \tag{4}$$

$$\widehat{n}_L(l) = \frac{n_L(l) - \min(n_L)}{\max(n_L) - \min(n_L)}, \tag{5}$$

where $\min(n_H)$ and $\max(n_H)$ respectively are the minimum and maximum values of n_H for all the layers. Similarly, $\min(n_L)$ and $\max(n_L)$ are the minimum and maximum values of n_L.

We note that both values of $\widehat{n}_H(l)$ and $\widehat{n}_L(l)$ fall between 0 and 1.

For a specimen printed with the total number of layer $\mathcal{L}$, we calculate the average values $\overline{n}_H$ and $\overline{n}_L$, which are indicative of the specimen's overall quality as

$$\overline{n}_H = \frac{1}{\mathcal{L}} \sum \widehat{n}_H(l), \tag{6}$$

$$\overline{n}_L = \frac{1}{\mathcal{L}} \sum \widehat{n}_L(l). \tag{7}$$

3.4. Thermal image processing

The thermal-imaging (TI) camera acquires thermography data at a rate of 25 FPS, with a spatial resolution of 195 μm/pixel. Temperature measurements for a specimen are obtained by overlaying a mask onto the transformed thermal images. This mask can either be a user-defined or produced through an active contour (see Section 3.2). The image registration method described in Section 3.1 is used for this transformation process. For each thermal image, the temperature readings within the masked region are then extracted and used to calculate the average temperature, denoted as T_a. By compiling the average temperatures T_a, we obtain the layer's average temperature as a function of time during the printing process. In Figure 7(a), we show a snippet of the time series T_a for a layer of a specimen fabricated using parameter setting $\mathbb{P}_5$. Figure 7(b,c)

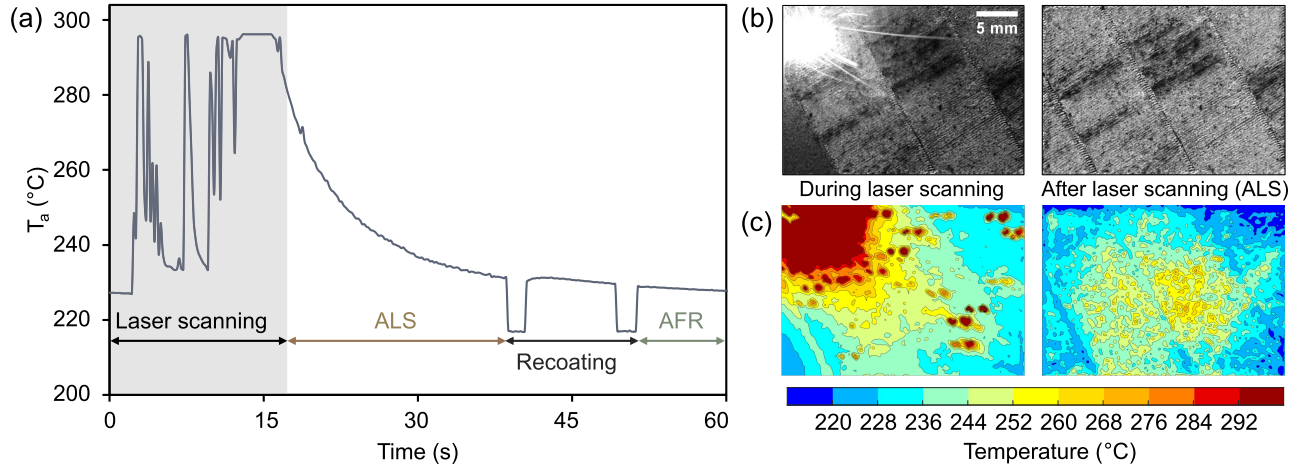

Figure 7. (a) Snippet of the time series T_a for a layer of a specimen fabricated using parameter setting $\mathbb{P}_5$. (b) Representative VI images of the same layer captured during laser scanning and after laser scanning (ALS). (c) Corresponding TI images showing the thermal distributions during the laser scanning and ALS stages.

show representative VI and TI images, respectively, of the same layer to illustrate the surface appearance and thermal state during and after laser scanning. Here, we note that the sudden dips in temperature in Figure 7(a) result from the recoater sweeping across the powder bed to apply a new powder layer and partially blocking the field of view of the thermal camera. The temperature readings during the sweeping motion of the recoater are therefore to be discarded.

For each layer, we obtain its representative temperature $\overline{T}(l)$ by averaging fifteen temperature readings right before recoating. We then calculate the overall mean temperature $\overline{T}_m$ for the printing of each specimen as

$$\overline{T}_m = \frac{1}{\mathcal{L}} \sum \overline{T}(l). \tag{8}$$

Here, $\overline{T}_m$ represents the mean ALS temperature across all layers of a specimen. We will seek to determine the relationship between the $\overline{T}_m$ and the surface features, characterised by $\overline{n}_H$ and $\overline{n}_L$ in Section 4.1. The algorithm for processing the thermal data is shown in Annex Figure A4.

4. Results and discussion

4.1. Correlation between surface appearance and temperature

To correlate a layer's surface appearance to its temperature and use this correlation to obtain optimum parameter ranges to minimise defects, we first analyze the surface features of cylindrical specimens fabricated with the printing parameter settings specified in Figure 2 and Table 2. We then examine the correlations between the quality indicators, $\overline{n}_L$ and $\overline{n}_H$, and the thermal information represented by $\overline{T}_m$. Figure 8 shows the ALS VI images, followed by the binarised images obtained from the HiPE and LoPE algorithms, and the corresponding TI images for selected specimens. The TI images, captured right before recoating, complement the VI-based surface analysis by providing a direct visualisation of the temperature distribution after laser scanning. From the observed features of the printed surfaces, we categorise surface characteristics into three major groups: (1) unsintered materials, which appear in shades of grey similar to the powder before laser scanning, (2) sintered materials, which are

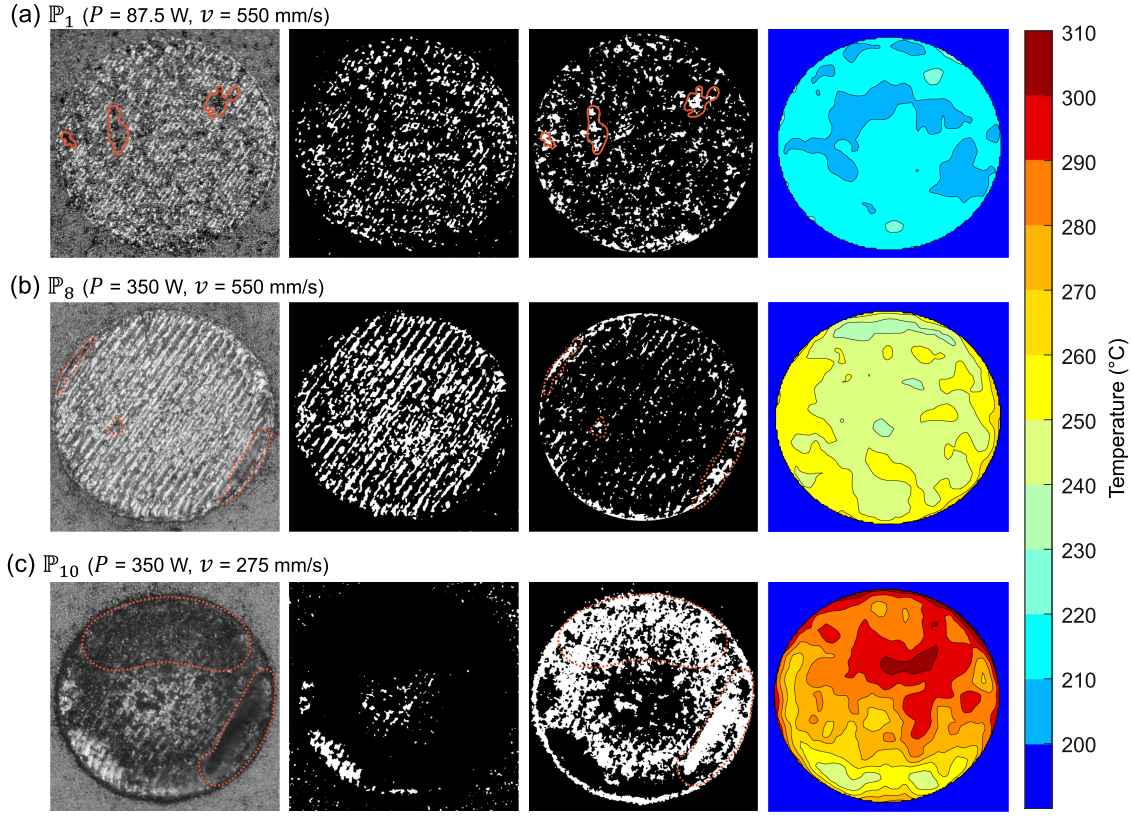

Figure 8. (a) Image taken after laser scanning, followed by binarised images processed with the HiPE and LoPE algorithms, respectively, and the corresponding TI image, captured right before recoating, for a specimen fabricated using parameter setting $\mathbb{P}_1$. The red curves highlight unsintered and re-deposited materials. (b) and (c): Similar snapshots taken for $\mathbb{P}_8$ and $\mathbb{P}_{10}$, respectively. Dotted curves in (c) highlight overheated areas due to high deposition energy density.

brighter than unsintered materials, and (3) overheated materials, which are darker than unsintered materials.

At the lowest laser power and moderate scanning speed, $\mathbb{P}_1$, the snapshot after laser scanning in Figure 8(a) shows disrupted scanning tracks with lighter shades and dark spots of re-deposited material among unsintered powder. These disrupted scanning tracks are revealed more clearly in the corresponding binarised HiPE image. The unsintered and the re-deposited materials, on the other hand, are better revealed in the corresponding binarised LoPE image where they appear in large white areas. The corresponding TI image shows a relatively low temperature field (below 220°C), indicating a lack of fusion.

At high laser power and moderate scanning speed, $\mathbb{P}_8$, the captured snapshot shown in Figure 8(b) reveals mostly continuous scanning tracks with narrow gaps between adjacent scanning tracks. The corresponding binarised HiPE image clearly shows these continuous scanning tracks while the LoPE image highlights clusterings of scanning track disruptions, especially at the edge of the scanned area due to high deposition energy density [18, 19]. The corresponding TI image exhibits a temperature field around 240°C, aligning with the optimal temperature range identified in Figure 9.

At high laser power and low scanning speed, $\mathbb{P}_{10}$, Figure 8(c) reveals a predominantly dark specimen surface. The increase in the deposition energy density leads to a notable rise in the number of active pixels within the binarised LoPE image, suggesting potential overheating. Conversely, the binarised HiPE image shows fewer active pixels. The corresponding TI image further supports the presence of potential overheating by showing elevated temperatures exceeding 280°C.

To determine the correlation between $\overline{T}_m$, $\overline{n}_L$, and $\overline{n}_H$ for ALS layers of all printed specimens, we show how they depend on the energy density E in Figure 9. We observe from Figure 9(a) that $\overline{T}_m$ increases roughly linearly with E. On the one hand, for parameter settings with low energy density ($\mathbb{P}_1$ and $\mathbb{P}_2$), we note that the characteristic features observed from ALS images mostly suggest lack of fusion (Figure 8(a)). Thus, we infer that the low energy densities produced by $\mathbb{P}_1$ and $\mathbb{P}_2$ are responsible for the low $\overline{T}_m$ and the resulting lack of fusion. On the other hand, the parameter settings with observed overheating characteristics ($\mathbb{P}_7$, $\mathbb{P}_9$, and $\mathbb{P}_{10}$) are associated with high energy density ($E \geq 2E_0$) and high temperature. As a result, we are able to extract an optimal temperature range, $219°C \leq \overline{T}_m \leq 243°C$, within which the observed indicators of overheating and lack of fusion are minimised.

We now examine the dependences of $\overline{n}_L$ and $\overline{n}_H$ on E, shown in Figure 9(b,c), respectively. We observe that the parameter settings associated with overheating ($\mathbb{P}_7$, $\mathbb{P}_9$, and $\mathbb{P}_{10}$) are well separated from others at $\overline{n}_L = 0.12$, a threshold extracted from Figure 9(b) by averaging the nearest values of $\overline{n}_L$ from overheating and non-overheating cases. Similarly, a threshold value of $\overline{n}_H < 0.38$ can be used to separate cases with overheating and lack of fusion from those with continuous scanning tracks, as shown in Figure 9(c).

We conclude that optimal printing conditions are achieved with $\overline{n}_L < 0.12$, $\overline{n}_H > 0.38$, and $219°C \leq \overline{T}_m \leq 243°C$. The parameter settings satisfying these conditions include $\mathbb{P}_3$, $\mathbb{P}_4$, $\mathbb{P}_5$, $\mathbb{P}_6$, and $\mathbb{P}_8$. These conditions can be imposed on in-situ monitoring quality indicators to prevent lack of fusion or overheating.

To validate the observed indicators of lack of fusion, overheating, and optimal print quality, we examine the mechanical properties of the printed specimens. Figure 10 shows the tensile strength σ plotted against

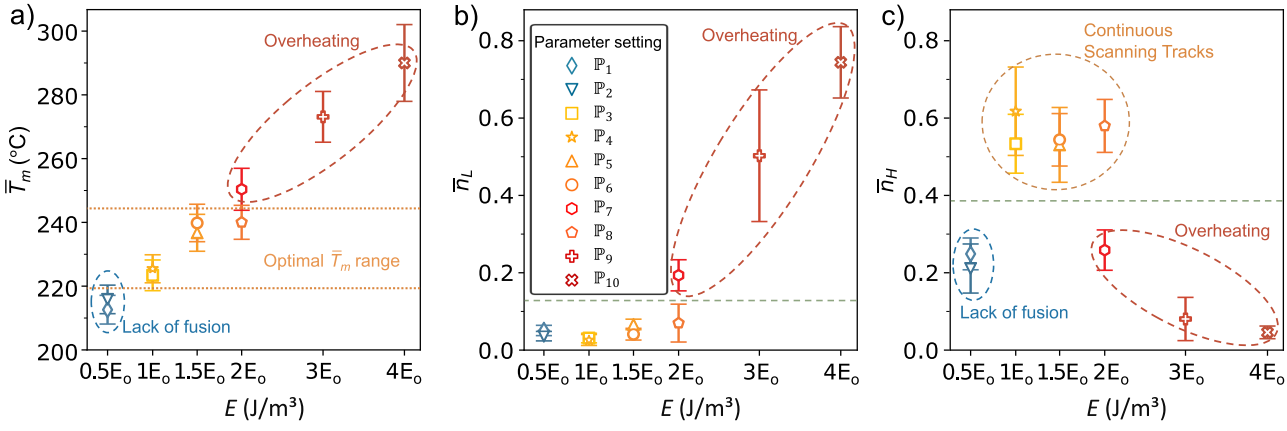

Figure 9. Correlation of $\overline{n}_L$, $\overline{n}_H$, $\overline{T}_m$ and energy density E through application of LoPE and HiPE algorithms to ALS images. Dashed green lines indicate quality boundaries for $\overline{n}_L$ and $\overline{n}_H$; dotted orange lines indicate optimal $\overline{T}_m$ range.

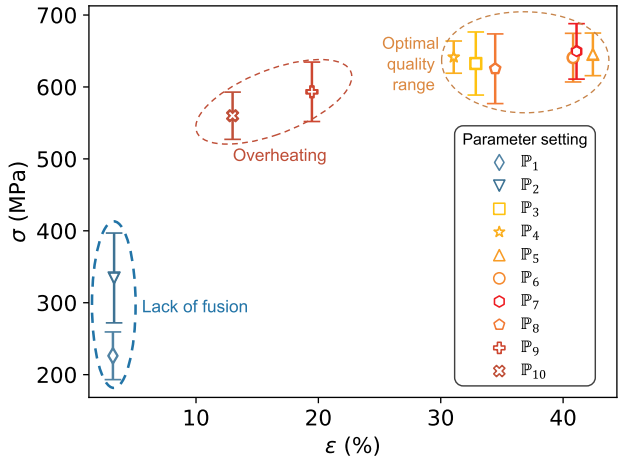

Figure 10. Tensile strength vs elongation at break for specimens fabricated with different parameter settings.

elongation at break ε for all specimens. Those exhibiting lack of fusion, as identified through surface and thermal analysis, showed both low tensile strength ($\sigma < 400$ MPa) and brittle behaviour, characterised by low elongation at break ($\varepsilon \approx 3\%$). Specimens affected by overheating displayed reduced mechanical performance due to thermal residual stresses, with moderate tensile strength ($\sigma \approx 580$ MPa) and limited ductility ($\varepsilon < 20\%$). In contrast, specimens within the identified optimal process window exhibited both high tensile strength ($\sigma > 600$ MPa) and high ductility ($\varepsilon > 30\%$). These tensile results confirm the effectiveness of the proposed quality indicators. We note that parameter setting $\mathbb{P}_7$, although classified as overheating based on surface features and elevated temperature, still exhibits high tensile performance. This indicates that $\mathbb{P}_7$ may still be subject to potential overheating, but it has not yet led to compromised mechanical properties. Nonetheless, the thresholds derived from VI and TI analysis provide a more conservative approach to quality assurance, enabling early detection of thermal anomalies before mechanical degradation becomes evident.

4.2. Detection of deformation caused by thermal residual stresses in overhanging specimens

We demonstrate the use of quality indicators in detecting deformation that occurs during the printing process of overhanging specimens. We fabricate six specimens with overhanging angles ranging from 30° to 75° (Figure 3) using parameter settings $\mathbb{P}_8$ ($P = 350$ W and $v = 550$ mm/s). As the lack of support structures becomes more significant with smaller overhanging angles, we anticipate deformation due to thermal residual stresses for specimen 1 ($\alpha = 30°$) and specimen 2 ($\alpha = 35°$) [20].

In Figure 11, we show several representative VI images captured from specimens of different overhanging angles. We observe two distinct features for specimens with low overhanging angles, e.g. specimen 1 ($\alpha = 30°$) and 2 ($\alpha = 35°$). First, the surfaces after laser scanning (ALS) exhibit mostly continuous tracks on the left-hand side, i.e. the region without overhanging structure underneath, whereas the tracks are diminishing toward the right-hand side, i.e. the overhanging region. Second, the region with an overhanging structure underneath becomes darkened with highly irregular patterns, suggesting out-of-plane deformation of scanned layers. This deformation is further verified by the after recoating images (AFR) taken right after the ALS images: the sintered material on top of the overhanging region protrudes upwards and is left exposed even after a newly coated powder layer is applied. As a comparison, specimens with high overhanging angles, e.g. specimens 4 ($\alpha = 45°$) and 6 ($\alpha = 75°$), display mostly continuous laser scanning tracks, without any notable deformation. The AFR images for specimens 4 and 6 show no protruding features on top of the overhanging region, aside from the edge effect at the specimen corners [18, 19].

In Figure 12, we show the layer-wise evolution of surface morphology and thermal distribution. As printing progresses from layer 80 to layer 198, the VI images reveal increasing surface darkening and irregularities in the overhanging regions of specimen 1 ($\alpha = 30°$) and specimen 2 ($\alpha = 35°$), suggesting the development of out-of-plane deformation. The corresponding TI images show a significant rise in temperature, particularly in the later layers, indicating heat accumulation. Specimen 3 ($\alpha = 40°$) shows mild signs of overheating, with localised darkening in the VI images and elevated temperatures in the TI images. In contrast, specimens 4 to 6 ($\alpha = 45°$ to 75°) exhibit mostly continuous scanning tracks in the VI images and relatively uniform temperature distributions in the TI images, suggesting stable thermal conditions without apparent thermal deformation. These observations support the use of quality indicators for detecting early-stage deformation during the build process of parts with complex geometries.

Figure 13 presents the dependencies of $\overline{n}_L$ and $\overline{T}_m$ on α at the late stage of printing the overhanging specimens, i.e. using the ALS images of the last 20 layers of the print job. We focus on the late stage of printing in which anomalies caused by overheating and thermal deformation are more prominent. Using the conditions obtained for the quality indicator $\overline{n}_L$, i.e. specimens unaffected by overheating have $\overline{n}_L < 0.12$, we infer that those printed with an $\alpha > 40°$ are not susceptible

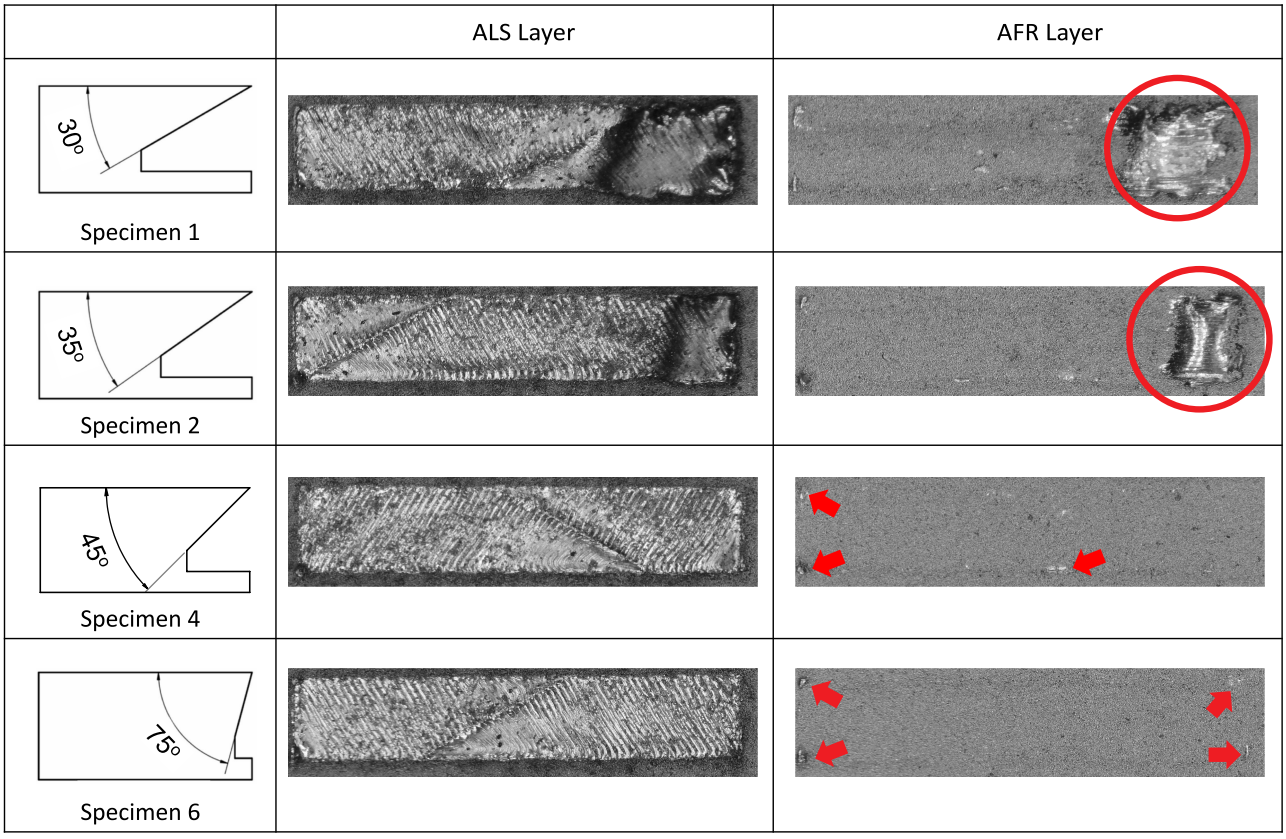

Figure 11. ALS and AFR VI images at layer 194 for specimens 1, 2, 4 and 6. Red circles highlight regions protruding above the recoated layer in AFR VI images of specimens 1 and 2. Red arrows in the AFR VI images of specimens 4 and 6 indicate edge elevations accumulated during laser scanning. All specimens are fabricated using parameter setting $\mathbb{P}_8(P = 350\,\text{W}, v = 550\,\text{mm/s})$.

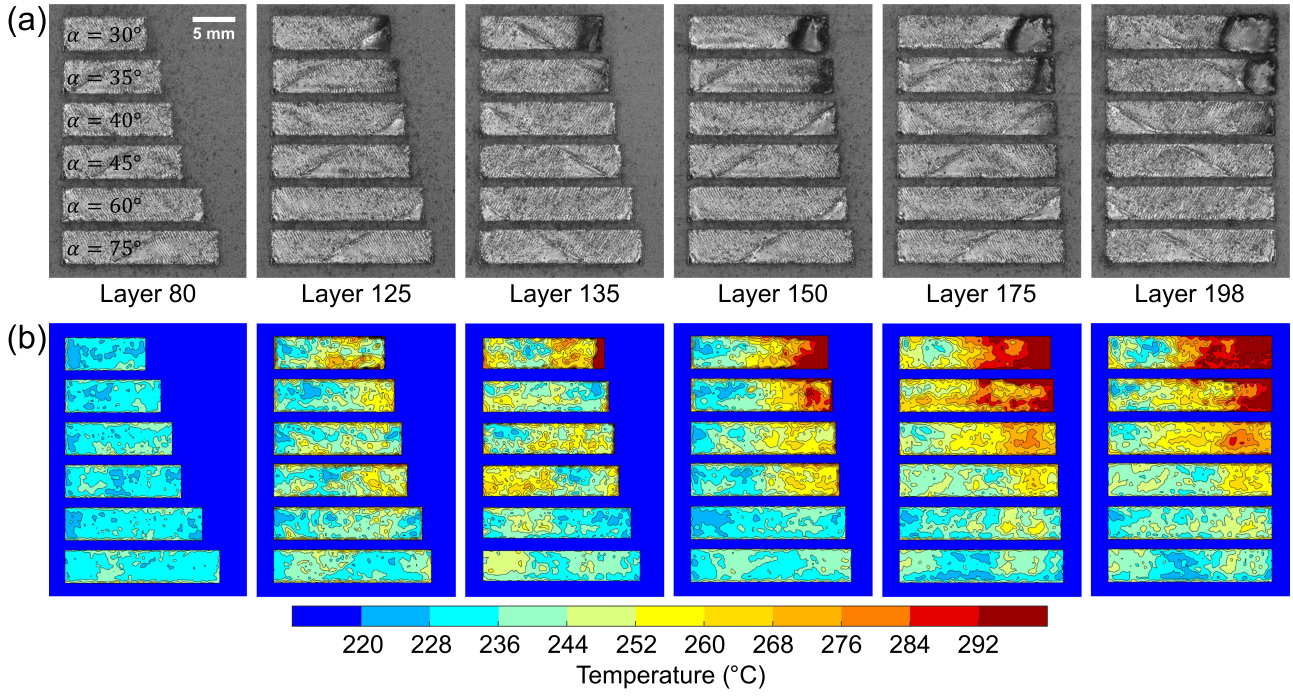

Figure 12. (a) VI images and (b) corresponding TI images of overhanging specimens captured at different layers.

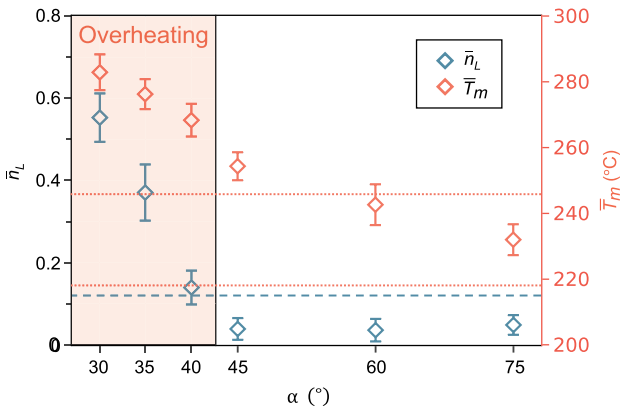

Figure 13. Relationships of $\bar{n}_L$ and $\bar{T}_m$ with overhanging angle α for the last 20 layers of the overhanging specimens. Dashed lines denote the quality boundaries for $\bar{n}_L$; dotted red lines indicate optimal $\bar{T}_m$ range.

to overheating and thermal deformation. Indeed, this is consistent with our observations obtained from VI images for specimens 4, 5, 6, i.e. those with $\alpha > 40^\circ$, that there is negligible deformation detected in both ALS and AFR images during the printing process, as shown in Figure 11.

Furthermore, we observe a decline in $\bar{T}_m$ with increasing α, reinforcing that specimens with smaller angles are more prone to overheating and subsequent thermal deformation. We note that for the specimen with $\alpha = 45^\circ$, $\bar{n}_L < 0.12$ is achieved but $\bar{T}_m \approx 255^\circ$C, which falls outside of the optimum temperature range $219^\circ\text{C} \leq \bar{T}_m \leq 243^\circ\text{C}$ identified from the analysis of cylindrical specimens. This discrepancy may result from the proximity of the specimens during the printing process: the heat generated from the specimens with lower α may dissipate to those with higher α and affect their mean temperature. Nonetheless, the optimum range of $\bar{T}_m$ still may serve as an important indicator for overheating it correctly predicts the overheating cases ($\alpha \leq 40^\circ$) and those without overheating ($\alpha \geq 60^\circ$). As a result, from the analysis of overhanging specimens, we demonstrate that our algorithms effectively extract and quantify overheating features using VI images and TI data, facilitating detection of part deformation caused by thermal residual stresses.

5. Conclusions

This paper presents a quantitative framework that fuses visible-light and thermal imaging data to formulate layer-wise quality indicators for laser powder bed fusion (L-PBF) processes. We developed image processing algorithms, namely High-Intensity Pixel Enhancement (HiPE) and Low-Intensity Pixel Enhancement (LoPE), to extract the surface shades either brighter or darker than the powder material from the VI images. By analyzing the number of active pixels in the binarised images, we correlate surface shades with potential anomalies. Additionally, we developed an algorithm to extract thermal metrics for each layer from TI data.

We demonstrated the correlation between printing quality and parameter settings through the analysis of two specimen sets. Our examination of cylindrical specimens showcased the effectiveness of the proposed algorithms and analytical approach in quantifying printing anomalies, such as overheating and lack of fusion, with optimal conditions characterised by low LoPE pixel counts ($\bar{n}_L < 0.12$) and high HiPE pixel counts ($\bar{n}_H > 0.38$), along with moderately stabilised temperatures ($219^\circ\text{C} \leq \bar{T}_m \leq 243^\circ\text{C}$). For specimens with overhangs, we further demonstrated our methodology and successfully identified geometric deformations caused by thermal residual stresses.

We validated our approach through tensile testing. Specimens printed with optimal parameter settings achieved both high tensile strength ($\sigma > 600$ MPa) and high ductility ($\varepsilon > 30\%$). In contrast, specimens exhibiting lack of fusion showed significantly reduced tensile strength ($\sigma < 400$ MPa) and brittle behaviour ($\varepsilon \approx 3\%$). Specimens affected by overheating maintained moderate tensile strength ($\sigma \approx 580$ MPa) but exhibited reduced ductility ($\varepsilon < 20\%$).

The proposed in-process monitoring system (IMS) and data fusion approach enable real-time, layer-wise identification of surface anomalies and defects during L-PBF processes. This research has the potential to scale up by integrating machine learning or deep learning techniques for enhanced anomaly detection in additive manufacturing processes.

Disclosure statement

No potential conflict of interest was reported by the author(s).

Funding

This research is supported by the National Research Foundation, Prime Minister's Office, Singapore under its Medium-Sized Centre funding scheme, and The Center for Environmental Intelligence (CEI) at VinUniversity, Vietnam.

ORCID

Allen Hum Jun Wee http://orcid.org/0000-0002-1072-2301
Truong Do http://orcid.org/0000-0003-1873-9789
Ngoc Vu Nguyen http://orcid.org/0000-0003-1778-0923
Tuan Tran http://orcid.org/0000-0002-5132-6495

Data availability statement

The authors confirm that the data supporting the findings of this study are available within the article [and/or] its supplementary materials.

References

[1] Attaran M. Additive manufacturing: the most promising technology to alter the supply chain and logistics. J Serv Sci Manag. 2017;10(03):189–206.

[2] Spears TG, Gold SA. In-process sensing in selective laser melting (slm) additive manufacturing. Integr Mater Manuf Innov. 2016;5(1):16–40. doi: 10.1186/s40192-016-0045-4

[3] Clijsters S, Craeghs T, Buls S, et al. In situ quality control of the selective laser melting process using a high-speed, real-time melt pool monitoring system. Int J Adv Manuf Technol. 2014;75(5):1089–1101. doi: 10.1007/s00170-014-6214-8

[4] Fox JC, Lane BM, Yeung H. Measurement of process dynamics through coaxially aligned high speed near-infrared imaging in laser powder bed fusion additive manufacturing. In: Thermosense: thermal infrared applications XXXIX, Vol. 10214; SPIE; 2017. p. 34–50.

[5] Foster B, Reutzel E, Nassar A, et al. Optical, layerwise monitoring of powder bed fusion. In: 2014 International Solid Freeform Fabrication Symposium; University of Texas at Austin, Austin, TX; 2015.

[6] Grasso M, Laguzza V, Semeraro Q, et al. In-process monitoring of selective laser melting: spatial detection of defects via image data analysis. J Manuf Sci Eng. 2017;139(5):051001. doi: 10.1115/1.4034715

[7] Scime L, Beuth J. Using machine learning to identify in-situ melt pool signatures indicative of flaw formation in a laser powder bed fusion additive manufacturing process. Addit Manuf. 2019;25:151–165.

[8] Caltanissetta F, Grasso M, Petro S, et al. Characterization of in-situ measurements based on layerwise imaging in laser powder bed fusion. Addit Manuf. 2018;24:183–199.

[9] Zhang Y, Fuh JY, Ye D, et al. In-situ monitoring of laser-based pbf via off-axis vision and image processing approaches. Addit Manuf. 2019;25:263–274.

[10] Lu QY, Nguyen NV, Hum AJW, et al. Identification and evaluation of defects in selective laser melted 316l stainless steel parts via in-situ monitoring and micro computed tomography. Addit Manuf. 2020;35:101287.

[11] Nguyen NV, Hum AJW, Do T, et al. Semi-supervised machine learning of optical in-situ monitoring data for anomaly detection in laser powder bed fusion. Virtual Phys Prototyp. 2023;18(1):e2129396. doi: 10.1080/17452759.2022.2129396

[12] Krauss H, Eschey C, Zaeh M. Thermography for monitoring the selective laser melting process. In: 2012 International Solid Freeform Fabrication Symposium; University of Texas at Austin, Austin, TX; 2012.

[13] Bartlett JL, Heim FM, Murty YV, et al. In situ defect detection in selective laser melting via full-field infrared thermography. Addit Manuf. 2018;24:595–605.

[14] Lu QY, Nguyen NV, Hum AJ, et al. Optical in-situ monitoring and correlation of density and mechanical properties of stainless steel parts produced by selective laser melting process based on varied energy density. J Mater Process Technol. 2019;271:520–531. doi: 10.1016/j.jmatprotec.2019.04.026

[15] Hrkac T, Kalafatic Z, Krapac J. Infrared-visual image registration based on corners and hausdorff distance. Scand Conf Image Anal (SCIA). 2007;4522:383–392.

[16] Rahman MM, Karim AZ. Comparative analysis of image registration using pixel wavelet and translation method. J Electr Electron Eng. 2015;5:23–33.

[17] Kass M, Witkin A, Terzopoulos D. Snake: active contour models. Int J Comput Vis. 1988;1:321–331. doi: 10.1007/BF00133570

[18] Valente EH, Gundlach C, Christiansen TL, et al. Effect of scanning strategy during selective laser melting on surface topography, porosity, and microstructure of additively manufactured ti-6al-4v. Appl Sci. 2019;9(24):5554. doi: 10.3390/app9245554

[19] Yasa E, Deckers JH, Craeghs T, et al. Investigation on occurrence of elevated edges in selective laser melting. In: International Solid Freeform Fabrication Symposium; University of Texas at Austin, Austin, TX; 2009.

[20] Kruth JP, Deckers JH, Yasa E, et al. Assessing and comparing influencing factors of residual stresses in selective laser melting using a novel analysis method. Proc Inst Mech Eng B: J Eng Manuf. 2012;226:980–991. doi: 10.1177/0954405412437085

Annex

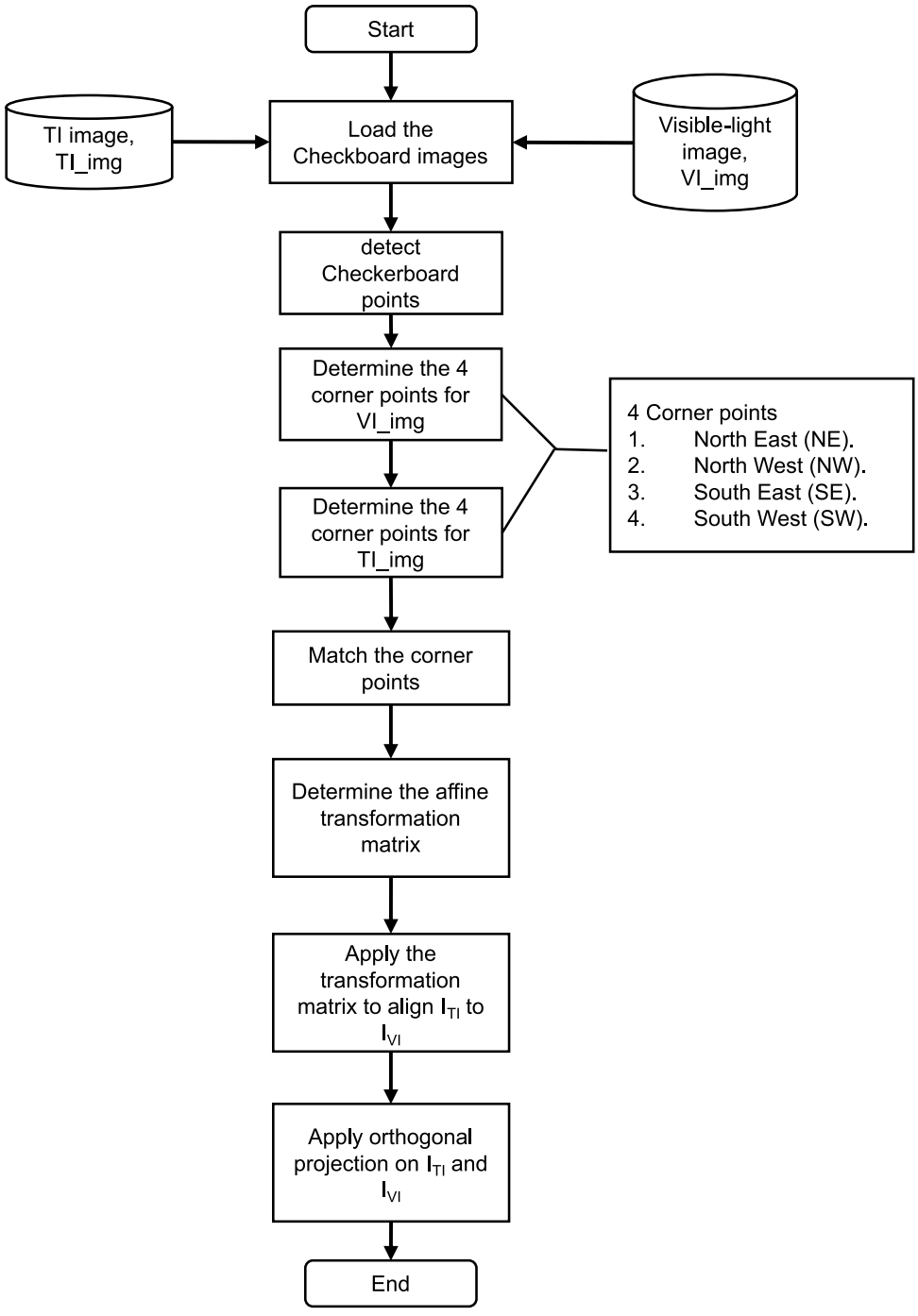

Figure A1. Algorithm for image registration.

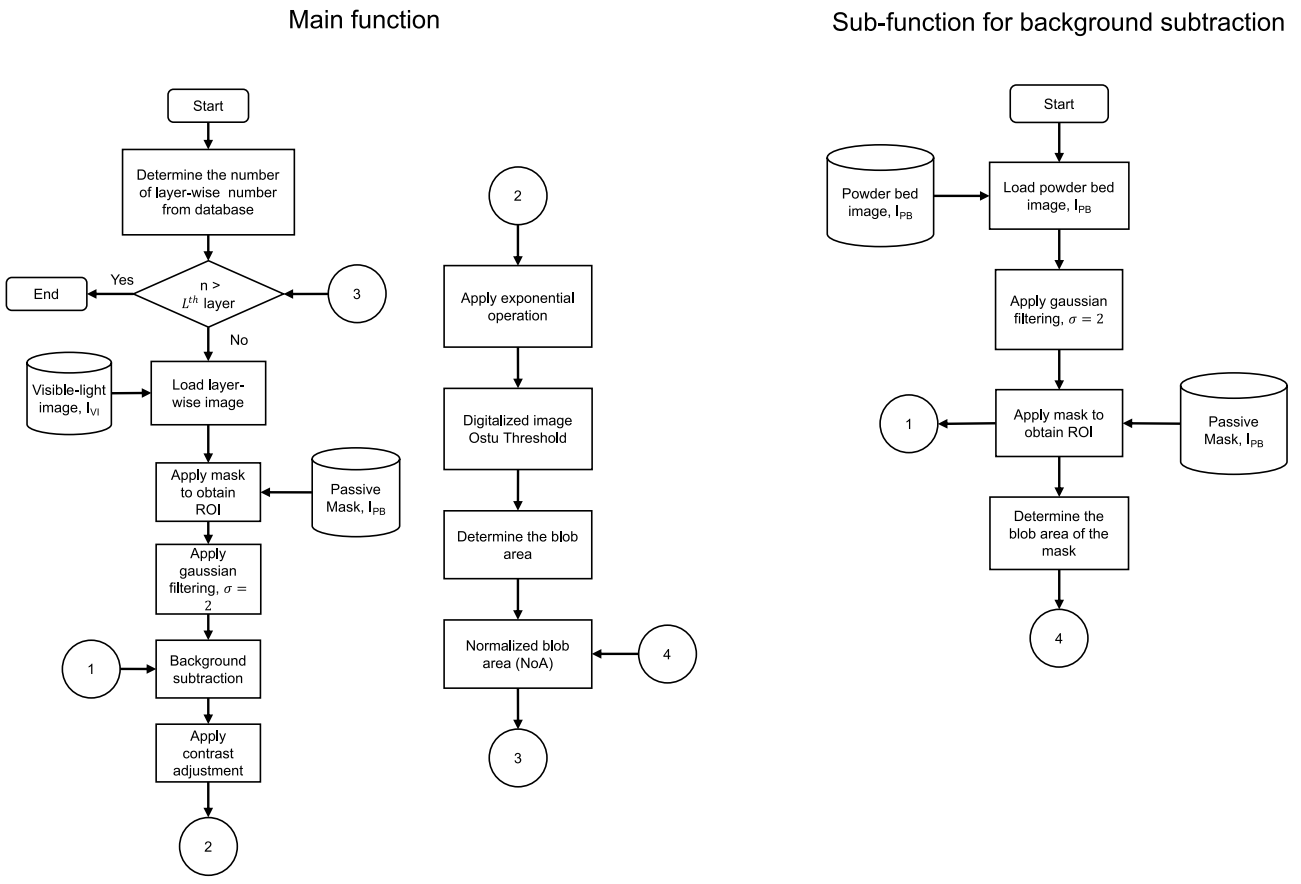

Figure A2. HiPE algorithm.

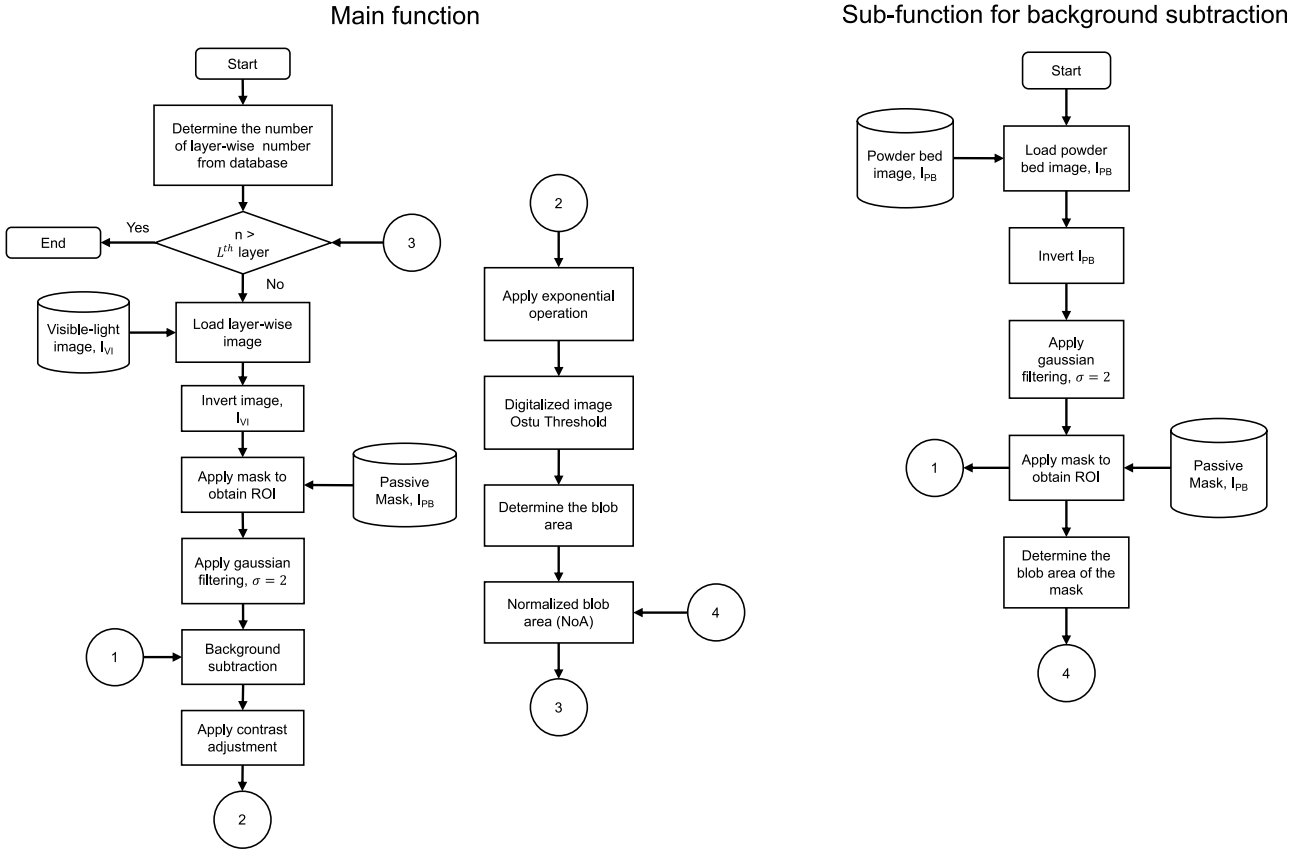

Figure A3. LoPE algorithm.

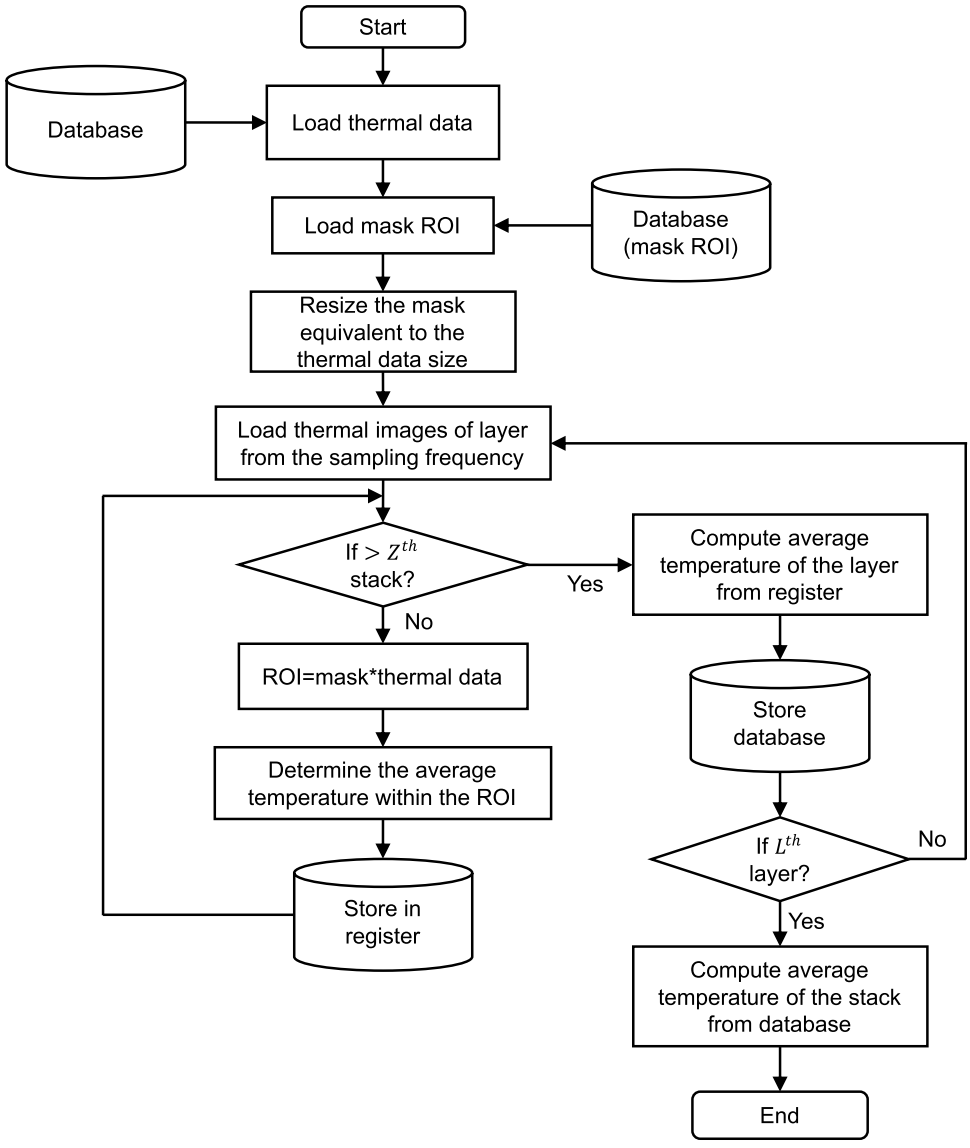

Figure A4. Algorithm to process the thermal data.